*Journal of Nano- and Electronic Physics*
Vol. **18** No 5, 05027(8pp) (2026)

*Журнал нано- та електронної фізики*
Том **18** № 5, 05027(8cc) (2026)

OPEN ACCESS

## REGULAR ARTICLE

# Spectral Dependence of the Effective Photoconductivity of Crystalline Silicon Containing Amorphous Inclusions of Different Morphologies

S.V. Babychenko*, O.Yu. Babychenko

*Kharkiv National University of Radio Electronics, 61166 Kharkiv, Ukraine*

(Received 15 June 2026; revised manuscript received 17 October 2026; published online 28 October 2026)

This study investigates the effective photoconductivity of a crystalline silicon structure containing both spherical and cylindrical amorphous inclusions. A combined numerical and analytical framework was developed in which the wavelength-dependent concentrations of photogenerated carriers in the constituent phases were obtained by solving the steady-state carrier continuity equations, accounting for optical generation, diffusion, bulk recombination, and interfacial carrier losses. The phase-specific photoconductivities were homogenized using the self-consistent Bruggeman effective medium approximation, incorporating the phase volume fractions, depolarization factors, and inclusion geometry. Calculations were performed over the wavelength range of 500-1100 nm for structural disorder parameters $\gamma = 0.05$, 0.10, and 0.15 eV and total amorphous-phase volume fractions of 5-15 %. The calculated photoconductivity of monocrystalline silicon was found to reach approximately 0.105 S·m$^{-1}$ near 880-900 nm. The corresponding maxima for the heterogeneous structures are approximately 0.097, 0.089, and 0.080 S·m$^{-1}$, representing reductions of 7.6 %, 15.2 %, and 23.8 %, respectively. The crystalline matrix governs the overall spectral profile, whereas structural disorder broadens the long-wavelength response of the amorphous phase. Inclusion geometry appreciably affects the local photoconductivity; however, its effect on the normalized effective photoconductivity remains below approximately 0.04 % for the configurations considered. The results demonstrate the applicability of the self-consistent Bruggeman effective medium approximation to multiphase photoconductive semiconductor structures containing inclusions of different geometries.

**Keywords:** Effective photoconductivity, Crystalline silicon, Amorphous inclusions. Bruggeman effective medium approximation, Semiconductor heterostructure, Structural disorder, Inclusion morphology.

DOI: 10.21272/jnep.18(5).05027 PACS numbers: 73.50.Pz, 78.66.Jg

## 1. INTRODUCTION

Crystalline semiconductors containing amorphous inclusions are structurally heterogeneous systems who's electronic and transport properties are governed by the phase-specific parameters, inclusion morphology, and interfacial properties. Amorphous regions may form because of technological processing, accumulated structural damage, or irradiation. In particular, the possibility of local amorphization of crystalline silicon induced by ion irradiation has been experimentally demonstrated [1-3]. Disruption of short- and medium-range order in the amorphous phase gives rise to spatial fluctuations in potential energy and the formation of localized band-tail states near the band edges. At the same time, dangling and distorted bonds may introduce deeper defect states within the mobility gap of the amorphous semiconductor. Additional electronic states may also form at amorphous-crystalline phase boundaries, particularly at the a-Si:H/c-Si interface [4, 5]. Depending on their energetic position, density, occupancy, and carrier-capture cross section, these states may participate in the trapping, release, and recombination of non-equilibrium charge carriers. Consequently, they modify the concentration, mobility, and lifetime of photogenerated carriers and, therefore, the photoconductivity of the material. Experimental studies of amorphous and microcrystalline silicon confirm the relationship between defect-state density, Fermi-level position, carrier lifetime, and photoconductivity [6].

The effective photoconductivity of such a heterogeneous structure is determined not only by the local conductivities of its constituent phases but also by the volume fractions, dimensions, shape, orientation, and spatial connectivity of the amorphous inclusions. Carrier transport across phase boundaries and interfacial recombination also exert a significant influence on the overall photoelectric response [1].

Research into these systems is motivated by the development of photosensitive multiphase materials, radiation-modified semiconductor structures, and amorphous-crystalline heterojunctions. Related a-Si:H/c-Si structures are of practical importance because they are widely employed for surface passivation and the formation of carrier-selective contacts in high-efficiency silicon heterojunction solar cells [7]. Establishing a quantitative relationship among the concentration, morphology, and orientation of amorphous inclusions, interfacial parameters, and effective photoconductivity therefore remains an important challenge in semiconductor physics and materials science.

* Correspondence e-mail: serhii.babychenko@nure.ua



© 2026 The Author(s). Journal of Nano- and Electronic Physics published by Sumy State University. This article is distributed under the terms and conditions of the Creative Commons Attribution (CC BY) license.

Cite this article as: S.V. Babychenko et al., *J. Nano- Electron. Phys.* 18 No 5, 05027 (2026) https://doi.org/10.21272/jnep.18(5).05027

## 2. BRUGGEMAN EFFECTIVE MEDIUM MODEL FOR A THREE-PHASE SEMICONDUCTOR HETEROSTRUCTURE

The effective photoconductivity of such a semiconductor structure depends on the concentration and mobility of photogenerated carriers, the degree of structural disorder, the volume fraction of the amorphous phase, and the morphology of the inclusions. Inclusion morphology is a key factor governing the electrical and photoconductive properties of the heterostructure. Spherical inclusions distributed in a macroscopically isotropic manner generally contribute to an effective isotropic conductivity. By contrast, cylindrical or elongated inclusions may produce different conductivities along and perpendicular to their principal axes, thereby giving rise to anisotropic transport. Their increased aspect ratio may also facilitate the formation of connected pathways and reduce the percolation threshold. An accurate numerical-analytical description of crystalline semiconductors containing amorphous inclusions must therefore account for the inclusion volume fraction, geometry, orientation, and interaction with the phase boundaries [8].

Effective medium theory (EMT), particularly the Maxwell-Garnett and Bruggeman formulations adapted to photogeneration conditions, provides a suitable framework for quantitatively describing the effective transport properties of such heterogeneous systems [9-12]. When combined with phase-specific models of photogeneration and carrier transport, these approaches can incorporate the electronic density of states, the energy distribution of trapping states, and interfacial properties, thereby establishing the relationship between inclusion morphology and effective photoconductivity.

The aim of this work is to investigate the influence of amorphous inclusions on the photoconductive properties of crystalline semiconductors and to develop a numerical–analytical framework for evaluating the effective photoconductivity of such heterostructures. Fig. 1 presents a schematic representation of the investigated structure and defines its principal geometrical parameters.

The self-consistent Bruggeman effective medium approximation was employed to quantitatively describe the photoconductivity of the investigated heterogeneous structure. Within this approach, each phase is treated as a constituent embedded in the as-yet-unknown effective medium, thereby providing a symmetric treatment of the local conductivities and volume fractions of all components. This formulation enables changes in the macroscopic transport properties to be described as a function of the phase composition. Generalization of the model through the introduction of depolarization factors, tensor components of conductivity, and percolation corrections makes it possible to account for the shape and orientation of the inclusions, anisotropic charge transport, and the formation of interconnected conductive pathways. The Bruggeman model therefore provides a physically grounded framework for evaluating the effective photoconductivity of multiphase semiconductor structures, including photosensitive, sensor, and thin-film systems.

For an $n$-phase system, the modified Bruggeman effective medium equation incorporating depolarization, geometrical, and percolation effects can be written in the general form

$$\sum_{j=1}^{n} f_j \frac{\sigma_j - \sigma_{eff}}{\sigma_{eff} + L_j G_j P_j(\sigma_i - \sigma_{eff})} = 0, \qquad (2.1)$$

where $\sigma_{eff}$ is the effective conductivity of the heterogeneous medium; $j$ denotes the phase index; $f_j$ is the volume fraction of phase $j$, subject to $\sum f_j = 1$; $\sigma_j$ is the local conductivity of phase $j$; $L_j$ is the corresponding depolarization factor; $G_j$ is the geometrical correction factor accounting for the inclusion morphology; and $P_j$ is the percolation correction factor.

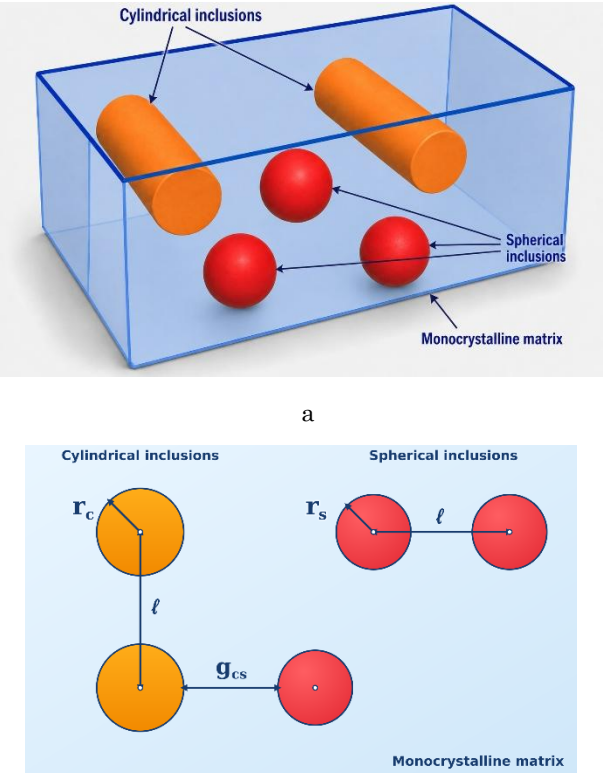



**Fig. 1** – Schematic representation of the structure (a) and definition of its geometrical parameters (b)

The percolation threshold in heterogeneous materials is strongly influenced by the shape and orientation of the inclusions. For isotropically distributed spherical inclusions, a critical volume fraction of approximately $f_c \approx 0.16 - 0.18$ is frequently reported [9, 12], although its precise value depends on the adopted microstructural model and the criterion used to define interparticle connectivity. For cylindrical or fibrous inclusions with an increased aspect ratio, the percolation threshold is generally lower than that of spherical particles, typically $f_c \sim 0.05 - 0.10$, because of the higher probability of forming continuous conductive pathways.

The effect of inclusion orientation is not universal. Parallel alignment may either increase or decrease the percolation threshold depending on the system geometry, transport direction, spatial distribution of the inclusions, and criterion for establishing interparticle contacts.

For a three-phase semiconductor heterostructure consisting of a crystalline matrix containing both spherical and cylindrical amorphous inclusions, the generalized Bruggeman equation can be written as follows:

$$f_c \frac{\sigma_c-\sigma_{eff}}{\sigma_{eff}+(LPG)_c\,(\sigma_c-\sigma_{eff})} + f_{sph} \frac{\sigma_{sph}-\sigma_{eff}}{\sigma_{eff}+(LPG)_{sph}\,(\sigma_a-\sigma_{eff})} + f_{cyl} \frac{\sigma_{cyl}-\sigma_{eff}}{\sigma_{eff}+(LPG)_{cyl}\,(\sigma_a-\sigma_{eff})} = 0 \quad (2.2)$$

In the present formulation, the depolarization, geometrical, and percolation factors for the crystalline silicon phase (c-Si) are taken as

$$L_{\mathrm{c}} \approx 1/3,\ G_{\mathrm{c}} = 1,\ P_{\mathrm{c}} = 1.$$

For the spherical amorphous inclusions, the corresponding factors are

$$L_{\mathrm{sph}} = 1/3,\ G_{\mathrm{sph}} = 1,\ P_{\mathrm{sph}} = 1.$$

For the cylindrical inclusions, the depolarization factors parallel and perpendicular to the cylinder axis are given by

$$L_{\mathrm{cyl},\parallel} \approx 0,\ L_{\mathrm{cyl},\perp} \approx 0.5,$$

respectively. The corresponding geometrical factors are taken as

$$G_{\mathrm{cyl},\parallel} \approx 1,\ G_{\mathrm{cyl},\perp} \approx 2,$$

while the percolation factor is $P_{\mathrm{cyl}} = 1$.

## 3. MATHEMATICAL DESCRIPTION OF PHOTOCONDUCTIVITY IN THE CONSTITUENT PHASES OF THE HETEROSTRUCTURE

To proceed from a qualitative description to a quantitative evaluation of the effective photoconductivity of the three-phase heterostructure – comprising a crystalline silicon matrix, amorphous cylindrical inclusions, and amorphous spherical inclusions – the local photoconductive parameters of each phase must first be determined. These parameters can be obtained by calculating the concentration of photogenerated charge carriers from the carrier continuity equations, accounting for generation, recombination, diffusion, and carrier losses at external surfaces and phase boundaries [13].

For the monocrystalline matrix and the cylindrical amorphous inclusions, assuming one-dimensional carrier transport along the ($x$)-axis, the carrier continuity equation can be written as follows:

$$\frac{\partial\cdot\Delta n_{m,a}}{dt} = D_{a,m}\frac{\partial^2\cdot\Delta n_{m,a}}{\partial x^2} - \frac{\Delta n_{m,a}}{\tau_{m,a}} + G_{m,a}\cdot exp(-\alpha_{m,a}x) \quad (3.1)$$

where $D_{a,m}$ is the carrier diffusion coefficient in the corresponding phase; $\Delta n_{m,a}$ is the excess carrier concentration; $\tau_{m,a}$ is the effective lifetime of photogenerated carriers in the corresponding phase; $G_{m,a}$ is the optical generation rate per unit volume; and $\alpha_{m,a}$ is the optical absorption coefficient.

Under steady-state illumination

$$\frac{\partial\cdot\Delta n_{m,a}}{dt} = 0.$$

In the low-injection regime and under the quasineutrality approximation,

$$\delta n_i \approx \delta p_i \equiv \Delta n$$

The carrier-transport problem therefore reduces to the steady-state ambipolar diffusion equation:

$$D_{a,m}\frac{d^2\Delta n_{m,a}}{dx^2} - \frac{\Delta n_{m,a}}{\tau_{m,a}} + G_{m,a}(x) = 0,\ \ 0 < x < d_m. \quad (3.2)$$

where $d_m$ is the thickness of the semiconductor sample.

The boundary conditions for the monocrystalline silicon matrix can be written as follows:

$$D_m\frac{d\Delta N_m}{dx}\,|_{x=0} = S_m\Delta N_m(0), \quad (3.3)$$

$$D_m\frac{d\Delta N_m}{dx}\,|_{x=d_m} = S_m\Delta N_m(d_m). \quad (3.4)$$

where $\mathrm{S}_m$ is the surface recombination velocity at the boundaries of the monocrystalline silicon wafer.

The boundary conditions for the cylindrical amorphous inclusions can be expressed as follows:

$$D_a\frac{\partial\Delta n_a}{\partial x}\Big|_{x=r} = S_a\cdot\Delta n(r)\,; \quad (3.5)$$

$$D_a\frac{\partial\Delta n_a}{\partial x}\Big|_{x=l} = -S_a\Delta n(l). \quad (3.6)$$

where $\mathrm{S_a}$ is the interfacial recombination velocity of charge carriers at the amorphous-crystalline phase boundary; $r$ is the radius of the amorphous inclusion; and $l$ is the center-to-center distance between adjacent amorphous inclusions.

The first boundary condition describes the recombination of photogenerated carriers at the lateral surface of the cylindrical amorphous inclusion, characterized by the interfacial recombination velocity $S_a$, which depends on the electronic properties of the interface. The second condition follows from the symmetry of the problem and corresponds to zero carrier flux at the symmetry plane, where the excess-carrier concentration reaches an extremum. This formulation explicitly accounts for the fact that, in sufficiently long cylindrical inclusions, carrier losses are governed predominantly by recombination at the lateral amorphous-crystalline interface.

The general solution of Eq. (3.1) can be written as follows:

$$\Delta n_{m,a} = \frac{G_{m,a}\cdot\tau_{m,a}}{1-\alpha^2 L_{m,a}{}^2}\cdot\left(A_{m,a}\cdot exp\left(\frac{x}{L_{m,a}}\right) + B_{m,a}\cdot exp\left(-\frac{x}{L_{m,a}}\right) + exp(-\alpha\cdot x)\right), \quad (3.7)$$

where $L_{m,a}$ is the carrier diffusion length in the corresponding phase.

The photoconductivity of each individual phase is determined from

$$\Delta\sigma_{m,a} = q(\mu_n + \mu_p)\Delta n_{m,a} \quad (3.8)$$

where $q$ is the elementary charge; $\mu_n$ and $\mu_p$ are the electron and hole mobilities, respectively.

By applying the boundary conditions given in Eqs. (3.3) and (3.4), the following expressions for the coefficients $A_m$ and $B_m$ of the monocrystalline phase are obtained:

$$A_m = \frac{(S_m-\alpha_m D_m)\cdot\left(\frac{D_m}{L_m}+S_m\right)\cdot exp(-\alpha_m d_m)+(S_m+\alpha_m D_m)\cdot\left(\frac{D_m}{L_m}-S_m\right)\cdot exp\left(-\frac{d_m}{L_m}\right)}{\left(\frac{D_m}{L_m}-S_m\right)^2\cdot exp\left(-\frac{d_m}{L_m}\right)-\left(\frac{D_m}{L_m}+S_m\right)^2\cdot exp\left(\frac{d_m}{L_m}\right)}; \quad (3.9)$$

$$B_m = \frac{(S_m-\alpha_m D_m)\cdot\left(\frac{D_m}{L_m}-S_m\right)\cdot exp(-\alpha_m d_m)+(S_m+\alpha_m D_m)\cdot\left(\frac{D_m}{L_m}+S_m\right)\cdot exp\left(\frac{d_m}{L_m}\right)}{\left(\frac{D_m}{L_m}-S_m\right)^2\cdot exp\left(-\frac{d_m}{L_m}\right)-\left(\frac{D_m}{L_m}+S_m\right)^2\cdot exp\left(\frac{d_m}{L_m}\right)}; \quad (3.10)$$

Accordingly, applying the boundary conditions given in Eqs. (3.5) and (3.6) to the cylindrical amorphous inclusions yields:

$$B_c = exp\left(-\frac{r}{L_a}\right)\cdot\frac{exp\left(\frac{l}{L_a}\right)\cdot exp(-\alpha_a\cdot r)\cdot(S_a+D_a\cdot\alpha_a)\cdot\left(S_a+\frac{D_a}{L_a}\right)-exp\left(\frac{r}{L_a}\right)\cdot exp(-\alpha_a\cdot l)\cdot(S_a-D_a\cdot\alpha_a)\cdot\left(S_a-\frac{D_a}{L_a}\right)}{exp\left(-\frac{l}{L_a}\right)\cdot\left(S_a+\frac{D_a}{L_a}\right)^2-exp\left(\frac{l}{L_a}\right)\cdot exp\left(-\frac{2\cdot r}{L_a}\right)\cdot\left(S_a-\frac{D_a}{L_a}\right)^2}; \quad (3.11)$$

$$A_c = \frac{exp\left(-\frac{r}{L_a}\right)}{\frac{D_a}{L_a}-S_a}\cdot\left(exp(-\alpha_a\cdot r)\cdot(S_a+D_a\cdot\alpha_a)+exp\left(-\frac{r}{L_a}\right)\cdot\left(S_a+\frac{D_a}{L_a}\right)\cdot B\right). \quad (3.12)$$

In modeling the properties of hydrogenated amorphous silicon, the carrier diffusion parameters were adopted from published experimental data obtained using the steady-state photocarrier grating technique. Their dependence on temperature, photogeneration rate, and the distribution of localized states was taken into account in accordance with Refs. [14, 15].

For spherical amorphous inclusions, assuming spherical symmetry within the region $r_0 \le r \le l$, the steady-state radial continuity equation can be written as follows:

$$\frac{d^2\Delta n_a}{dr^2}+\frac{2}{r}\frac{d\Delta n_a}{dr}-\frac{\Delta n_a}{{L_a}^2}=-\frac{\tau_a G_a}{{L_a}^2} \quad (3.13)$$

subject to the following boundary conditions at the surfaces of the inclusions:

$$\frac{d\Delta p(r)}{dr}=\frac{\tau_a S_a}{{L_a}^2}\Delta n_a(r), \qquad \frac{d\Delta n_a(l)}{dr}=0 \quad (3.14)$$

The first boundary condition describes carrier recombination at the surface of the amorphous inclusion, whereas the second assumes that the photogenerated carrier concentration reaches its maximum at the midpoint between adjacent inclusions. Owing to its finite dimensions, a spherical inclusion has a relatively high surface-area-to-volume ratio; consequently, interfacial recombination can significantly affect the volume-averaged concentration of photogenerated carriers within the inclusion.

The optical generation rate in each phase is determined by its absorption coefficient and the local photon flux density. For monochromatic radiation with wavelength λ, the volumetric photogeneration rate can be expressed as follows:

$$G_{m,a}(x,\lambda)=\eta_{m,a}(\lambda)\,\alpha_{m,a}(\lambda)\,\Phi(\lambda)\exp[-\alpha_{m,a}(\lambda)x], \quad (3.15)$$

where $\eta_i(\lambda)$ is the photogeneration quantum yield and $\Phi(\lambda)$ is the photon flux incident on the corresponding phase.

For the crystalline silicon matrix, the absorption coefficient was adopted from the data reported in Ref. [16].

In the amorphous a-Si:H phase, the absorption edge exhibits different behavior owing to structural disorder, band-tail states, and the broadened nature of optical transitions.

According to Ref. [17], the general relationship between the density of states and the optical absorption coefficient of amorphous silicon can be expressed as follows:

$$\alpha_a(h\nu)=\frac{2\pi h}{c}\cdot\left(\frac{e}{m}\right)^2\frac{1}{h\nu}\int N(E)f(E)\cdot N(E+h\nu)(1\text{-}f(E_{h\nu}))P(E,E+h\nu)dE \quad (3.16)$$

where $f(E)$ is the Fermi-Dirac distribution function, and $P(\mathrm{E},\mathrm{E}+\mathrm{h}\nu)$ is the matrix element of the optical transition.

The conduction- and valence-band density-of-states functions for amorphous silicon, accounting for the degree of structural disorder, are given by [13]:

$$N_c(E)=\frac{\sqrt{2}\cdot m_c^{*3/2}}{\pi^2\cdot\hbar^3}\begin{cases}\sqrt{E-E_c}, & E\ge E_c+\frac{\gamma_c}{2}\\ \sqrt{\frac{\gamma_c}{2}}\cdot exp\left(-\frac{1}{2}\right)\cdot exp\left(\frac{E-E_c}{\gamma_c}\right), & E<E_c+\frac{\gamma_c}{2}\end{cases} \quad (3.17)$$

$$N_v(E)=\frac{\sqrt{2}\cdot m_v^{*3/2}}{\pi^2\cdot\hbar^3}\begin{cases}\sqrt{\frac{\gamma_v}{2}}\cdot exp\left(-\frac{1}{2}\right)\cdot exp\left(\frac{E_v-E}{\gamma_v}\right), & E\ge V_v-\frac{\gamma_v}{2}\\ \sqrt{E_v-E}, & E<E_v-\frac{\gamma_v}{2}\end{cases} \quad (3.18)$$

where $m_c^*$ is the effective electron mass in the conduction band; $m_v^*$ is the effective hole mass in the valence band; $E_c$ is the energy at the bottom of the disordered conduction band; $E_v$ is the energy at the top of the disordered valence band; $E_c+\frac{\gamma_c}{2}$ is the crossover energy between the parabolic and exponential regions of the conduction-band density of states; $E_v-\frac{\gamma_v}{2}$ is the corresponding crossover energy for the valence band; $\gamma_v$ is the valence-band-tail width; and $\gamma_c$ is the conduction-band-tail width. The parameters $\gamma_c$ and $\gamma_v$ characterize the degree of structural disorder.

## 4. SPECTRAL PHOTOCONDUCTIVITY OF THE HETEROSTRUCTURE: NUMERICAL RESULTS AND DISCUSSION

Fig. 2 shows the calculated spectral dependence of the optical absorption coefficient for different degrees of structural disorder, as described in Ref. [17].

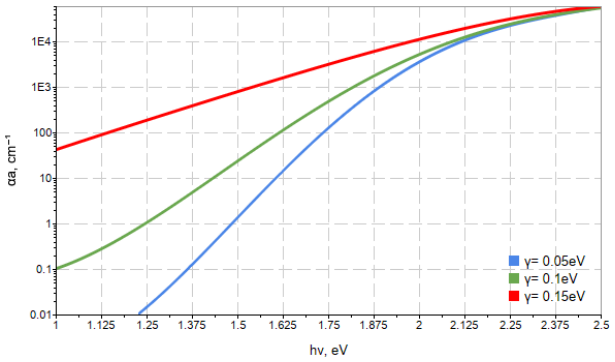



**Fig. 2** – Spectral dependence of the optical absorption coefficient for the case of $\gamma_c = \gamma_v$

Fig. 3 shows the calculated spectral dependence of the photoconductivity of the monocrystalline matrix.

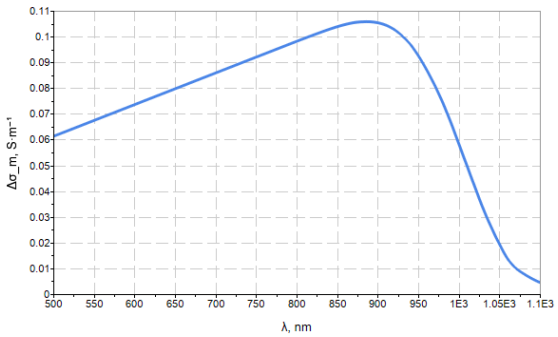
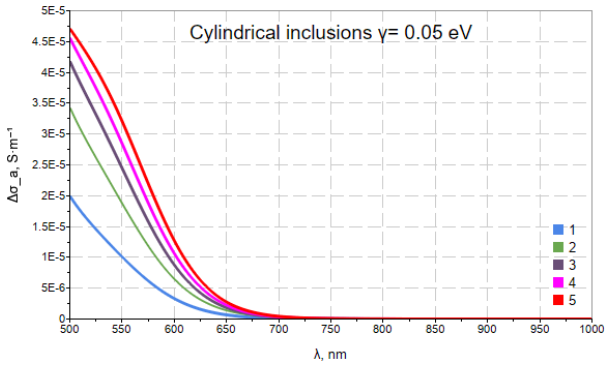



**Fig. 3** – Spectral dependence of the photoconductivity of the crystalline matrix

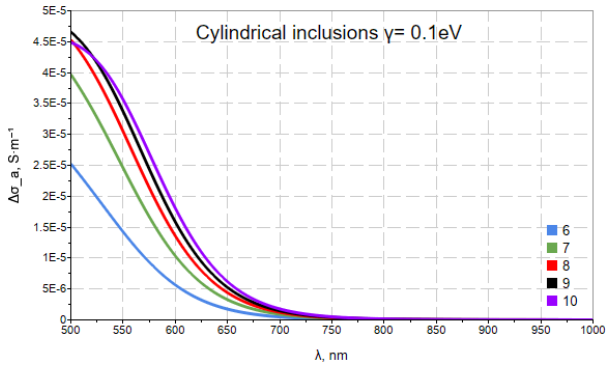
Fig. 4 presents the calculated spectral dependences of the photoconductivity of the structure containing amorphous inclusions for different degrees of structural disorder, $\gamma = 0.05, 0.1$ and $0.15$ eV, and different geometrical configurations of the inclusions. Within the adopted model, these values of $\gamma$ were assigned total amorphous-phase volume fractions of 5 %, 10 %, and 15 %, respectively. The cylindrical and spherical amorphous inclusions were assumed to have equal volume fractions of 2.5 %, 5.0 %, and 7.5 % for each inclusion type, respectively. The geometrical dimensions of the inclusions were determined from the specified volume fractions. Curves 1-15 correspond to different spatial and geometrical configurations of the spherical and cylindrical amorphous inclusions, whose parameters are listed in Table 1.

**Table 1** – Geometrical configurations of the amorphous inclusions

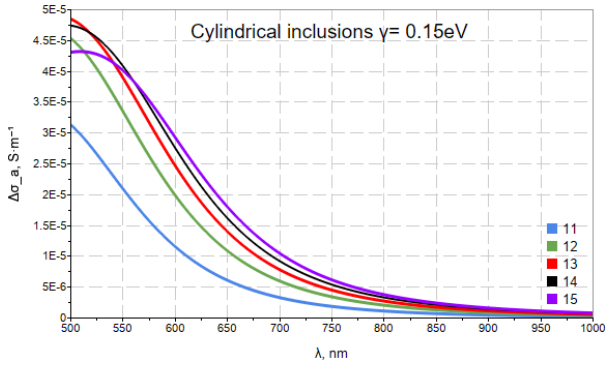
| № trace | $\gamma$ | $r_c$, nm | $r_s$, nm | $l$, nm | $g_{cs}$, nm |
|---|---|---|---|---|---|
| 1 | 0.05 | 22 | 45 | 250 | 109 |
| 2 | 0.05 | 49 | 99 | 550 | 240 |
| 3 | 0.05 | 75 | 154 | 850 | 371 |
| 4 | 0.05 | 102 | 208 | 1150 | 501 |
| 5 | 0.05 | 142 | 290 | 1600 | 698 |
| 6 | 0.1 | 31 | 57 | 250 | 88 |
| 7 | 0.1 | 69 | 125 | 550 | 193 |
| 8 | 0.1 | 107 | 194 | 850 | 299 |
| 9 | 0.1 | 145 | 262 | 1150 | 405 |
| 10 | 0.1 | 201 | 365 | 1600 | 563 |
| 11 | 0.15 | 38 | 65 | 250 | 72 |
| 12 | 0.15 | 84 | 143 | 550 | 160 |
| 13 | 0.15 | 131 | 222 | 850 | 247 |
| 14 | 0.15 | 177 | 300 | 1150 | 334 |
| 15 | 0.15 | 247 | 418 | 1600 | 465 |




a



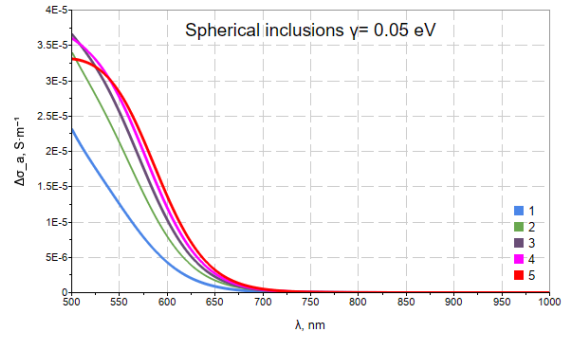

b



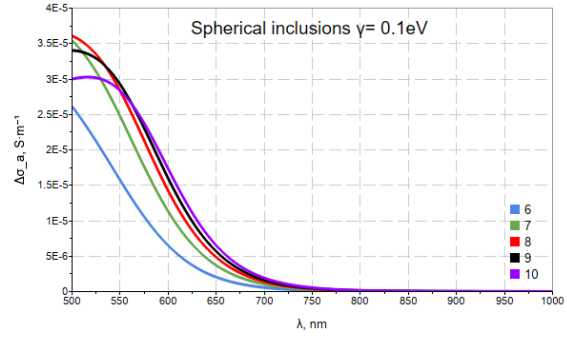

c

**Fig. 4** – Spectral dependences of the photoconductivity of cylindrical amorphous inclusions for different values of the structural disorder parameter: $\gamma = 0.05$ eV (a), $\gamma = 0.1$ eV (b), and $\gamma = 0.15$ eV (c). Curves 1–15 correspond to different geometrical configurations of the inclusions

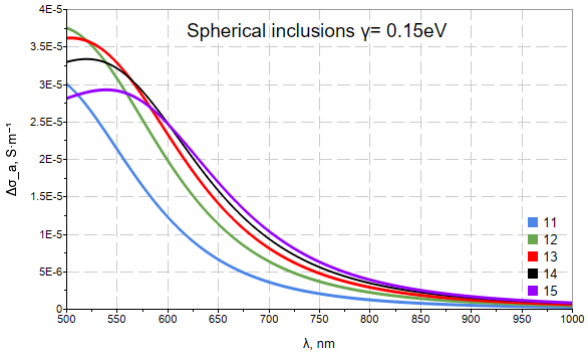
Fig. 5 presents the calculated spectral dependences of the photoconductivity of spherical amorphous inclusions for different values of the structural disorder parameter, $\gamma = 0.05, 0.1$ and $0.15$ eV, and various geometrical configurations of the structure.




a




b

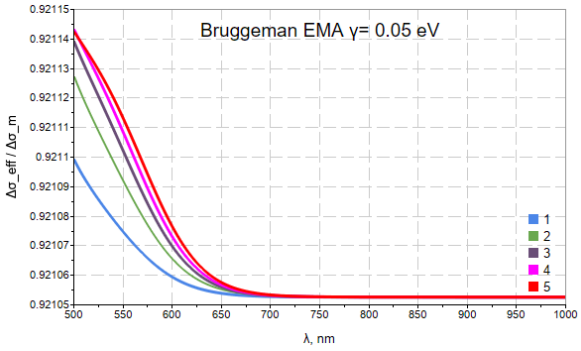



c

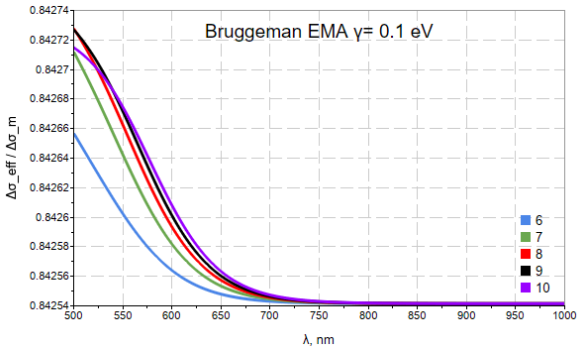
**Fig. 5** – Spectral dependences of the photoconductivity of spherical amorphous inclusions for different values of the structural disorder parameter: $\gamma = 0.05$ eV (a), $\gamma = 0.1$ eV (b), and $\gamma = 0.15$ eV (c). Curves 1-15 correspond to different geometrical configurations of the inclusions

Fig. 6 presents the calculated spectral dependences of the normalized effective photoconductivity of a semiconductor structure containing both cylindrical and spherical amorphous inclusions within a crystalline matrix. The calculations were performed using the self-consistent Bruggeman effective medium model for different values of the structural disorder parameter: $\gamma = 0.05, 0.1$ and $0.15$ eV

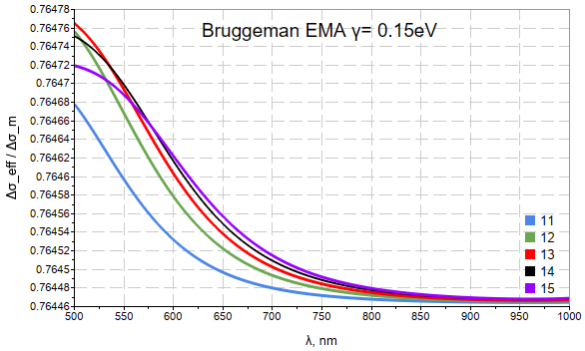
Fig. 7 presents the spectral dependences of the effective photoconductivity calculated using the self-consistent Bruggeman effective medium model. The geometrical parameters and volume fractions of the cylindrical and spherical amorphous inclusions were kept constant, while the structural disorder parameter was set to $\gamma = 0.05, 0.1$ and $0.15$ eV. The spectral dependence of the photoconductivity of monocrystalline silicon (c-Si) is also shown for comparison.




a




b




c

**Fig. 6** – Spectral dependences of the normalized effective photoconductivity of the semiconductor structure calculated using the Bruggeman model for $\gamma = 0.05$ eV (a), $\gamma = 0.1$ eV (b), and $\gamma = 0.15$ eV (c)

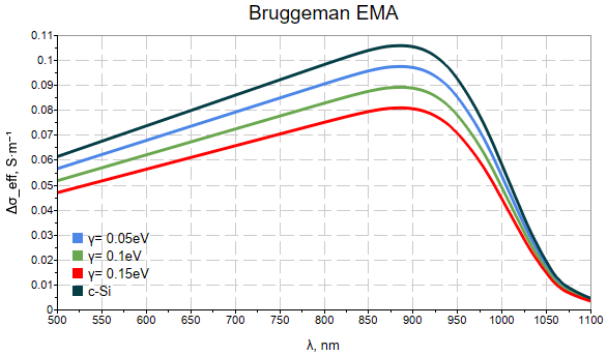



**Fig. 7** – Spectral dependences of the effective photoconductivity of the structure containing amorphous inclusions, calculated using the Bruggeman model, compared with the photoconductivity of the monocrystalline matrix

The calculations demonstrate that the spectral response of the heterogeneous structure is governed predominantly by the monocrystalline silicon matrix. The effective photoconductivity maximum remains within the wavelength range of $\lambda$ = 880-900 nm; however, the incorporation of the amorphous phase reduces its magnitude. For the cases considered, the maximum photoconductivity decreases from approximately 0.105 S·m$^{-1}$ for c-Si to 0.097, 0.089 and 0.080 S·m$^{-1}$, corresponding to relative reductions of approximately 7.6 %, 15.2 %, and 23.8 %, respectively. An increase in the degree of structural disorder within the amorphous phase broadens the long-wavelength tail of its photoconductivity spectrum. Nevertheless, the local photoconductivity of the amorphous inclusions remains approximately three orders of magnitude lower than that of the crystalline matrix. Consequently, the direct contribution of the amorphous phase to charge transport is negligible. Its influence on the macroscopic photoconductivity arises primarily from the replacement of a fraction of the more conductive crystalline matrix and from carrier recombination losses at the interphase boundaries. Variations in the absolute inclusion dimensions at a fixed relative geometry affect the local photoconductivity of the spherical and cylindrical phases by altering the ratio between the characteristic inclusion dimensions and the carrier diffusion length. However, the effect of the investigated geometrical configurations on the normalized effective photoconductivity of the entire structure does not exceed approximately 0.04 %. Within the investigated parameter range, the amorphous-phase volume fraction therefore has a substantially greater effect on the effective photoconductivity than the absolute dimensions of the inclusions.

## 5. CONCLUSION

A numerical-analytical framework was developed to determine the effective photoconductivity of a crystalline silicon structure containing both spherical and cylindrical amorphous inclusions. The proposed approach combines the calculation of the spatial distribution of photogenerated carriers within each constituent phase using the carrier continuity equations with the subsequent self-consistent homogenization of the local phase photoconductivities within the Bruggeman effective medium model.

The self-consistent Bruggeman model enables a quantitative description of the effective photoconductivity of a three-phase system comprising a crystalline matrix and spherical and cylindrical amorphous inclusions. Within this formulation, each phase is treated as a constituent of the effective medium. The incorporation of the phase volume fractions, local photoconductivities, depolarization factors, and geometrical factors allows the effects of the phase composition and inclusion morphology on the macroscopic photoelectric response to be represented. The obtained dependences demonstrate the applicability of the Bruggeman model to the self-consistent description of photoconductivity in crystalline semiconductor structures containing amorphous inclusions of different morphologies.

## REFERENCES


1. S. Torquato, *Random Heterogeneous Materials: Microstructure and Macroscopic Properties* (New York, NY, USA: Springer: 2002 https://doi.org/10.1007/978-1-4757-6355-3.
2. Yunshan Zhao, Xiangjun Liu, Ashutosh Rath, Jing Wu, Baowen Li, WuXing Zhou,Guofeng Xie, Gang Zhang, John T. L. Thong, *Sci. Rep.* **10**, 821 (2020) https://doi.org/10.1038/s41598-020-57514-9.
3. A. N. Dovbnya, V. P Yefimov, G. D. Pugachev, V. S. Dyomin, N A. Dovbnya, Yu. E. Gordienko, B G. Borodin, S. V. Babychenko, and T. A. Semenets, *New Technologies, nos.* **1–2 (7–8)**, (2005). [In Russian].
4. Y. Luo and A. J. Flewitt, *Phys. Rev. B* **109**, 104203 (2024) https://doi.org/10.1103/PhysRevB.109.104203.
5. 5. B. M. George, J. Behrends, A. Schnegg, T. F. Schulze, M. Fehr, L. Korte, B. Rech, K. Lips, M. Rohrmüller, E. Rauls, W. G. Schmidt, U. Gerstmann, *Phys. Rev. Lett.* **110**, 136803 (2013) https://doi.org/10.1103/PhysRevLett.110.136803.
6. O. Astakhov, R. Carius, F. Finger, Y. Petrusenko, V. Borysenko, D. Barankov, *Phys. Rev. B* **79**, 104205 (2009) https://doi.org/10.1103/PhysRevB.79.104205.
7. Xiaoning Ru, Miao Yang, Shi Yin, Yichun Wang, Chengjian Hong, Fuguo Peng, Yunlai Yuan, Chang Sun, Chaowei Xue, Minghao Qu, Jianbo Wang, Junxiong Lu, Liang Fang, Hao Deng, Tian Xie, Shengzhong (Frank) Liu, Zhenguo Li, Xixiang Xu, *Joule* **8**, No 4, 1092 (2024) https://doi.org/10.1016/j.joule.2024.01.015.
8. Oksana Babychenko, Olha Sushko, Serhii Babychenko, Volodymyr Logunov, Hennadii Bendeberya, *J. Nano-Electron. Phys.* **16** No 1, 01013 (2024) https://doi.org/10.21272/jnep.16(1).01013.
9. S. Kumar, H. Narayan, C. Diestel, J. Schmitz, J. Haunschild, S. Rein, and S. J. Rupitsch, *IEEE J. Photovolt.* **16** No 1, 113 (2026) https://doi.org/10.1109/JPHOTOV.2025.3619977.
10. M. Sahimi, *Applications of Percolation Theory*, 2nd ed. (Cham, Switzerland: Springer: 2023) https://doi.org/10.1007/978-3-031-20386-2.
11. F. Qin, M. Peng, D. Estevez, C. Brosseau, *J. Appl. Phys.* vol. **132**, 101101 (2022) https://doi.org/10.1063/5.0099072.
12. R. Nazarov, T. Zhang, M. Khodzitsky, *Photonics* **7** No 4, 113 (2020) https://doi.org/10.3390/photonics7040113.
13. O.Yu. Babychenko, A.G Pashchenko. *Telecommun. Radio Eng.* **77** No 2, 161 (2018) https://doi.org/10.1615/TelecomRadEng.v77.i2.70.
14. L. Kopprio, C. Longeaud, *Semiconduct. Sci. Technol.* **36**, No 12, 125003 (2021) https://doi.org/10.1088/1361-6641/ac271b.
15. L. Kopprio, C. Longeaud, J. Schmidt, *Semiconduct. Sci. Technol.* **34** No 4, 045010 (2019) https://doi.org/10.1088/1361-6641/ab0765.
16. M. A. Green, M. J. Keevers, *Progr. Photovolt.: Res. Appl.* **3** No 3, 189 (1995) https://doi.org/10.1002/pip.4670030303.
17. S. Babychenko, O. Babychenko, O Galat, *J. Nano-Electron. Phys.* **17** No 4, 04006 (2025) https://doi.org/10.21272/jnep.17(4).04006.

# Спектральна залежність ефективної фотопровідності кристалічного кремнію, що містить аморфні включення різної морфології

С.В. Бабиченко, О.Ю. Бабиченко

*Харківський національний університет радіоелектроніки, 61166 Харків, Україна*

У роботі вивчається ефективна фотопровідність структури на основі кристалічного кремнію, що містить аморфні включення сферичної та циліндричної форм. Було розроблено комбінований чисельно-аналітичний підхід, у межах якого концентрації фотогенерованих носіїв заряду в окремих фазах (як функції довжини хвилі) визначалися шляхом розв'язання стаціонарних рівнянь неперервності для носіїв. При цьому враховувалися процеси оптичної генерації, дифузії, об'ємної рекомбінації та втрат носіїв на межах розділу фаз. Ефективні параметри фотопровідності для кожної фази усереднювалися з використанням самоузгодженого наближення ефективного середовища Брюггемана, що враховує об'ємні частки фаз, фактори деполяризації та геометричні характеристики включень. Розрахунки проводилися в діапазоні довжин хвиль 500-1100 нм для параметрів структурного безладу $\gamma$ = 0,05, 0,10 та 0,15 еВ, при загальній об'ємній частці аморфної фази від 5 до 15 %. Встановлено, що для монокристалічного кремнію розрахункова фотопровідність досягає приблизно 0,105 См/м у діапазоні 880-900 нм. Відповідні максимальні значення для гетерогенних структур становлять приблизно 0,097, 0,089 та 0,080 См/м, що відповідає зниженню на 7,6 %, 15,2 % та 23,8 % відповідно. Кристалічна матриця визначає загальний спектральний профіль, тоді як структурний безлад призводить до розширення відгуку аморфної фази в довгохвильовій області. Геометрія включень суттєво впливає на локальну фотопровідність; однак її вплив на нормовану ефективну фотопровідність для розглянутих конфігурацій залишається на рівні менше 0,04 %. Отримані результати демонструють застосовність самоузгодженого наближення ефективного середовища Брюггемана до багатофазних напівпровідникових структур, що мають фотопровідні властивості та містять включення різної геометричної форми.

**Ключові слова:** Ефективна фотопровідність, Кристалічний кремній, Аморфні включення, Наближення ефективного середовища Брюггемана, Напівпровідникова гетероструктура, Структурний безлад, Морфологія включень.